Atomization and Sprays, 28(9):811–835 (2018)

GLOBAL CHARACTERIZATION OF THE SPRAY FORMATION PROCESS

M.F. Trujillo,* S. Gurjar, M. Mason, & A. Agarwal

Department of Mechanical Engineering, University of Wisconsin-Madison, 1513 University Ave., Madison, WI 53706, USA

*Address all correspondence to: M.F. Trujillo, Department of Mechanical Engineering, University of Wisconsin-Madison, 1513 University Ave., Madison, WI 53706, USA, E-mail: mtrujillo@wisc.edu

Original Manuscript Submitted: 7/7/2018; Final Draft Received: 10/24/2018

The interphase momentum coupling and growth in interfacial mass flow rate corresponding to liquid jet injection into a quiescent gas are studied in the present work via highly-resolved simulations. It is shown that the spray formation process is composed of three regimes. In the first regime, which is closest to the nozzle, the surface of the jet undergoes interfacial perturbations and breakup; however, the internal liquid core remains intact, and the interphase momentum exchange is weak. In the second regime, primary atomization occurs, resulting in the breakup of the entire jet. Besides the creation of relatively large amounts of interfacial area, this second regime is characterized by a huge increase in the momentum coupling between the gas and liquid phases. In the last regime, both phases merge into a quasi-equilibrium state, where the atomization process is essentially complete, and both phasic velocities converge to a unique average value. In a subsequent analysis, this unique value is shown to be given by $(U_{inj}\rho_L\Omega_L)/(\rho_L\Omega_L + \rho_G\Omega_G)$.

KEY WORDS: *breakup, near-field spray, interphase momentum, interfacial area, inter-Foam*

1. INTRODUCTION

The current study aims to explore the characteristics of interphase momentum transfer and interfacial area throughout the atomization and post-atomization regions of a liquid jet being injected into a quiescent gas environment. The near-field region is where the initial conditions of the spray are set, and where the strongest exchange of momentum takes place between the gas and liquid phases. This momentum exchange has a direct effect in the air entrainment characteristics and in the subsequent mixing of fuel vapor and air. The level of air entrainment impacts the flow patterns and local stoichiometry of the flow, which in turn affects the performance and emission levels of combustion systems (Briffa and Dombrowski, 1966; Ricou and Spalding, 1961; Zhao, 2009). Hence, it represents a key region for continued investigation.

Due to the large difference between the liquid and gas velocity field in the near-field region, this part of the domain is characterized by large shear rate values, leading to the violent production of a droplet cloud surrounding the liquid core. As a result, the density of the cloud has rendered this region very difficult to visualize with traditional optical techniques. In response, experimental efforts based on ultra-fast X-ray techniques (Wang et al., 2008), ballistic imaging (Linne et al., 2006), X-ray radiography (Kastengren et al., 2014), among other advanced methods continue to be developed and improved. Currently, however, the combination of fast-moving liquid structures with micron-level features in the near-field still poses significant

challenges to visualization and quantification. Additionally, if the interest also includes velocity characteristics, such as is the case here, an attractive alternative is the use of high-fidelity numerical simulations.

The high-fidelity simulation efforts, often referred to as DNS, are commonly based on implicit interface representation techniques such as level set or volume-of-fluid (VoF) (Sethian and Smereka, 2003; Tryggvason et al., 2011). These numerical techniques have been used to study various aspects of the atomization process. For instance, in the work of Herrmann et al. (2010), the effect of air/liquid density ratio on primary atomization for liquid jet in crossflow is studied, where it is reported that this density ratio has a significant influence in jet penetration and droplet size. Shinjo and Umemura (2010, 2011a,b) have numerically and theoretically investigated the jet head and surrounding gas and liquid flow structures by employing a combined VoF and level set method. Among other findings, they report that the jet head and liquid core play an interacting role in the creation of the interfacial disturbances. Instabilities in the azimuthal direction have been analyzed in the work of Jarrahbashi and Sirignano (2014), expanding the causes of atomization beyond the Rayleigh-Taylor instability. Ling et al. (2017) studied the development of 3D and 2D instabilities and subsequent spray formation in a gas–liquid mixing layer. One of the conclusions from the work is the need to numerically resolve the development of interfacial waves, as this was found to be crucial in predicting correct droplet size distributions. Using a similar planar liquid sheet geometry, Zandian et al. (2017) identified three distinct atomization cascades at early breakup time and categorized these cascades on a gas Weber number versus liquid Reynolds number map. While the simulation strategies underpinning these aforementioned efforts were mostly developed 10 to 15 years ago, they are still being refined and improved to deal with the difficulties of simulating atomization [e.g., Chiodi and Desjardins (2017)].

In the present work, we employ a VoF (Deshpande et al., 2012) simulation strategy to better understand the momentum coupling between the gas and liquid phases in the near-nozzle region. As previously suggested, this region is characterized by the fiercest momentum interaction producing a large degree of liquid breakup. The results from the present work show that the spray formation process can be characterized by three distinct domains or regimes. In terms of distance from the nozzle exit, the first domain is characterized by a relatively mild growth in the interfacial area, which is quantified in the present work by an interfacial mass flow rate. In this first region, the momentum exchange between both phases is relatively weak. The second domain is characterized by vigorous breakup and the disintegration of the liquid core, which leads to a strong transfer of momentum from the liquid to the surrounding gas. And in the last domain, this strong momentum exchange leads to a diminishing difference between the liquid and gas phase mean velocities, which asymptotically approach a unique value. Atomization has largely subsided in this last regime.

In what follows, the numerical framework employed in the simulations is presented in Section 2. A description of the computational setup and definition of the metrics is provided in Section 3 followed by some comments regarding numerical resolution issues in Section 3.1. The main results are then presented in Section 4 along with an analysis of the interphase momentum exchange in Section 4.2. An overall summary of our findings and final conclusions are included in Section 5.

2. GOVERNING EQUATIONS AND NUMERICAL DESCRIPTION

The computations reported in this work are performed using an algebraic VoF solver, InterFoam, which forms a part of a larger open-source distribution of computational mechanics solvers and

C++ libraries of OpenFOAM. The solver employs finite volume discretization on colocated grids for the solution of two-phase incompressible flows and benefits from various discretization strategies.

In a previous publication from our group (Deshpande et al., 2012), a detailed description of the algorithm and performance analysis was carried out with regard to the kinematics of advection, dynamics in an inertia-dominated regime, and dynamics in the surface-tension-dominated regime. With respect to the kinematics of advection, the performance of InterFoam is comparable to the other algebraic VoF schemes of Gopala and van Wachem (2008), as well as to the coupled level set VoF method of Sussman and Puckett (2000), and the ELVIRA method of Pilliod and Puckett (2004). However, when compared with schemes using a higher order of geometric reconstruction (Aulisa et al., 2003; Rider and Kothe, 1998; Xiao et al., 2011), InterFoam incurs noticeably larger errors. Nevertheless, algebraic treatment renders a significant algorithmic simplicity to the solver, while the advection errors can be addressed with adequate grid resolution. The solver ensures mass conservation rigorously, as is expected from a VoF algorithm. With respect to dynamics, the solver performs well in both capillary-dominated and inertia-dominated flows. Additionally, the solver shows no instability and is able to deal with very large density ratios [$\mathcal{O}(10^3)$ and larger] accurately.

A brief overview of the code is given here. More detailed explanations can be found in Deshpande et al. (2012). In essence, the following conservation equation is being solved:

$$\frac{\partial \alpha_i}{\partial t} + \nabla \cdot (\mathbf{u}\alpha_i) = 0, \tag{1}$$

where α_i is the liquid fraction pertaining to an arbitrary computational cell Ω_i. Since α_i has sharp gradients in the interfacial region, care has to be taken in computing the flux terms. Hence, the following version of the above equation is solved:

$$\frac{\alpha_i^{n+1} - \alpha_i^n}{\Delta t} + \frac{1}{|\Omega_i|} \sum_{f \in \partial\Omega_i} (F_u + \lambda_M F_c) = 0, \tag{2}$$

which appears here in discretized form. Indices n and i denote time levels and spatial referencing, respectively. Subscript f (face) refers to a cell-face quantity. The fluxes are defined as

$$F_u = \phi_f^n \alpha_{f,\text{upwind}}^n \quad \text{and} \quad F_c = \phi_f^n \alpha_f^n + \phi_{rf}^n \alpha_{rf}^n (1 - \alpha_{rf}^n) - F_u, \tag{3}$$

where $\phi_f^n = \mathbf{u}_f^n \cdot \mathbf{S}_f$, and $\mathbf{S}_f$ is the outward normal vector corresponding to a given cell (not normalized). The face value of $\mathbf{u}_f^n$ is obtained using the second order central scheme. In the flux term, F_u, the upwind value for the liquid fraction is denoted by $\alpha_{f,\text{upwind}}^n$. With respect to F_c, α_f^n is determined from the second order vanLeer scheme (Van Leer, 1974). The remaining quantities comprised the compressive flux, $\phi_{rf}^n \alpha_{rf}^n (1 - \alpha_{rf}^n)$. Here

$$\phi_{rf}^n = \min_{f' \in \Omega_i} \left(\frac{|\phi_{f'}^n|}{|\mathbf{S}_{f'}|}, U_{rf,\max} \right) (\mathbf{n}_f \cdot \mathbf{S}_f), \quad \text{where} \quad U_{rf,\max} = \max_{f \in \Omega} \left[\frac{|\phi_f^n|}{|\mathbf{S}_f|} \right]. \tag{4}$$

Lastly, the variable α_{rf}^n is obtained using the *interfaceCompression* scheme native to OpenFOAM (Deshpande et al., 2012; OpenFOAM User Guide, 2008; Rusche, 2002). The delimiter λ_M adjusts the treatment given to the advection of α_i. In regions of the domain that are sufficiently removed from the interface, the cells that reside here have values of $\lambda_M = 0$ at all of

their faces. This region is denoted as Ω_{sp} and it can be either gas or liquid. In Ω_{sp}, Eq. (2) can be written as

$$\frac{\alpha_i^{n+1}-\alpha_i^n}{\Delta t} = -\frac{1}{|\Omega_i|}\sum_{f\in\partial\Omega_i}\phi_f^n\alpha_{f,\text{upwind}}^n = -\frac{1}{|\Omega_i|}\alpha_{f,\text{upwind}}^n\sum_{f\in\partial\Omega_i}\phi_f^n \cong 0, \tag{5}$$

since $\alpha_{f,\text{upwind}}^n$ is uniform at all respective faces, and $\sum_{f\in\partial\Omega_i}\phi_f^n = 0$ to the extent that incompressibility is enforced in the code. This essentially keeps α_i values the same from one time level to the next for cells in Ω_{sp}. The complementary region to Ω_{sp} is Ω_{int}, the interfacial region. In this part of the domain, λ_M departs from zero and the flux receives contributions from F_c as defined in Eq. (3). This helps to a great extent the mitigation of numerical diffusion at the interface. In numerical tests concerning the advection of a discontinuous profile, for instance a Heaviside function, the treatment given above for the liquid fraction performs noticeably better than TVD schemes with regard to the preservation of the sharpness of the α field.

With respect to momentum, the following equation is solved:

$$\begin{aligned}\frac{\partial\rho\mathbf{u}}{\partial t} + \nabla\cdot(\rho\mathbf{u}\otimes\mathbf{u}) = -\nabla p_d + [\nabla\cdot(\mu\nabla\mathbf{u}) + \nabla\mathbf{u}\cdot\nabla\mu] \\ - \mathbf{g}\cdot\mathbf{x}\nabla\rho + \int_{\Gamma(t)}\sigma\kappa\delta(\mathbf{x}-\mathbf{x}_s)\mathbf{n}d\Gamma(\mathbf{x}_s),\end{aligned} \tag{6}$$

where the surface tension coefficient is given by σ, local curvature by κ, the gas–liquid interface by $\Gamma(t)$, the 3D Dirac Delta function by $\delta(\mathbf{x}-\mathbf{x}_s)$, and $\mathbf{x}_s$ is the integration variable over $\Gamma(t)$. In the finite volume discretization, the density and viscosity fields are regularized by

$$\rho = \rho_L\alpha + \rho_G(1-\alpha) \quad \text{and} \quad \mu = \mu_L\alpha + \mu_G(1-\alpha), \tag{7}$$

where ρ_L and ρ_G are, respectively, the liquid and gas phase densities, and μ_L and μ_G are, respectively, the liquid and gas phase dynamic viscosities. Additionally, the continuum surface tension model of Brackbill et al. (1992) is employed, rendering

$$\int_{\Gamma(t)\cap\Omega_i}\sigma\kappa\delta(\mathbf{x}-\mathbf{x}_s)\mathbf{n}d\Gamma(\mathbf{x}_s) = \int_{\Omega_i}\sigma\kappa\nabla\alpha dV. \tag{8}$$

The solution of the momentum equation [Eq. (6)] is obtained via a PISO (Issa, 1986) iteration procedure. A predictor velocity is first constructed and then corrected to ensure momentum balance and mass continuity. Explicit formulation of the predictor velocity is a two-step process, where first the viscous, advective, and temporal terms in the momentum equation are used to generate a cell centered vector field, which is then projected to cell faces using a second order scheme. Contributions from surface tension and gravity terms are then added, concluding the predictor formulation. This procedure enforces a consistent discretization of surface tension and pressure gradient (Deshpande et al., 2012; Francois et al., 2006).

Within the correction procedure, the pressure contribution is added to the flux of predictor velocity and mass conservation is invoked to yield a Poisson equation for pressure. The linear system is then solved using a preconditioned conjugate gradient method, with diagonal incomplete cholesky as the preconditioner to advance the pressure and velocity fields to a new iteration level within the PISO loop. This completes one correction step. In the present work, we have used three such steps to arrive at the time advanced solution, $\mathbf{U}^{n+1}$, pd^{n+1}.

3. SIMULATION SETUP AND DEFINITIONS OF METRICS

The physical situation under consideration and the associated computational domain is depicted in Fig. 1. Two different sets of cases are considered to provide us with a broader range of injection conditions. The first set consists of injection from a nozzle having a 90 μm diameter (D), where the inlet velocity profile is spatially uniform with a magnitude of U_{inj}, a flat hat profile. The domain extends over a space given by $L_x \times L_y \times L_z = 4400$ μm $\times$ 4400 μm $\times$ 32,000 μm, where the z-direction coincides with the injection orientation. Octree refinement is employed, where the finest resolution is $D/\Delta x = 24$ or $\Delta x = 3.75$ μm, and this level of resolution is maintained in a region extending out from the nozzle 90D (8100 μm) along the z-axis and 7D (630 μm) along the transverse and normal directions. Outside this refined region, the grid resolution drops gradually from $\Delta x = 3.75$ μm to $\Delta x = 120$ μm in the far-field.

The second set of cases have a much smaller nozzle diameter, namely $D = 30$ μm. The inlet velocity profile is $U_z(r) = U_{inj}\,(1 - r/R)^{1/7}$, where U_{inj} is varied as indicated below. The main reason for the smaller diameter cases is to allow for much tighter numerical resolution. For this second set of cases, the cell size in the spray region is $\Delta x = 1.875$ μm for 30, 40, and 50 m/s computations and $\Delta x = 1.5$ μm for the 70 m/s computations. To improve the efficiency of the calculations a telescoping grid strategy is employed, where the radial extent in the near-nozzle region is 60 μm and in the far-field, it is 160 μm. This configuration is the one that is displayed in Fig. 1. Both sets of calculations have the onset of injection occurring at $t = 0$ s with the rate of injection remaining constant throughout the calculation. Most of the cases are based on isooctane as the working fluid, but also JP-5 and the hydroprocessed renewable naval fuel HRD-F76 are employed. Additionally, the density ratio is also varied. The associated physical properties employed as well as a description of the various cases are provided in Tables 1, 2, 3, and 4. In the text that follows, subscripts L and G denote liquid and gas, respectively.

To inspect the type of atomization behavior resulting from simulations performed under the conditions presented in Table 4, the simulation parameters are placed within the atomization regime map of Reitz and Bracco (1986) as shown in Fig. 2. This regime map classifies the atomization process in term of liquid-based Reynolds and Ohnesorge numbers beginning with the mild Rayleigh regime and ending in the full atomization mode. For the calculations of current interest, we span the second wind-induced regime into the atomization regime.

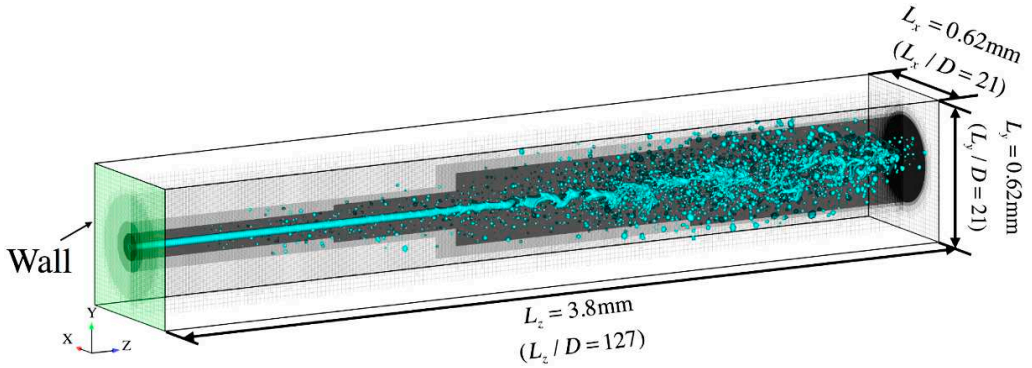

FIG. 1: Depiction of the physical domain employed in the 30 μm diameter cases along with a sample calculation corresponding to $U_{inj} = 50$ m/s. A no-slip wall boundary condition for the velocity is prescribed at the wall surrounding the nozzle exit.

TABLE 1: Physical properties for isooctane

Liquid density	$\rho_L = 688.03$ kg/m^3
Liquid viscosity	$\mu_L = 4.78 \times 10^{-4}$ kg/(m·s)
Gas density	$\rho_G = 50$ kg/m^3 (Cases 1–7)
	$\rho_G = 33$ kg/m^3 (Case 8)
	$\rho_G = 25$ kg/m^3 (Case 9)
Gas viscosity	$\mu_G = 1.88 \times 10^{-5}$ kg/(m·s)
Coefficient of surface tension	$\sigma = 0.02$ kg/s^2
Density ratio	$\hat{\rho} = \rho_L/\rho_G = 13.76$ (Cases 1–7)
	$\hat{\rho} = \rho_L/\rho_G = 20.8$ (Case 8)
	$\hat{\rho} = \rho_L/\rho_G = 27.5$ (Case 9)
Viscosity ratio	$\hat{\mu} = \mu_L/\mu_G = 25.4$

TABLE 2: Physical properties for JP-5

Liquid density	$\rho_L = 800$ kg/m^3
Liquid viscosity	$\mu_L = 1.48 \times 10^{-3}$ kg/(m·s)
Gas density	$\rho_G = 50$ kg/m^3
Gas viscosity	$\mu_G = 1.88 \times 10^{-5}$ kg/(m·s)
Coefficient of surface tension	$\sigma = 0.0249$ kg/s^2
Density ratio	$\hat{\rho} = \rho_L/\rho_G = 16$
Viscosity ratio	$\hat{\mu} = \mu_L/\mu_G = 78.7$

TABLE 3: Physical properties for HRD-76

Liquid density	$\rho_L = 781$ kg/m^3
Liquid viscosity	$\mu_L = 4.69 \times 10^{-3}$ kg/(m·s)
Gas density	$\rho_G = 50$ kg/m^3
Gas viscosity	$\mu_G = 1.88 \times 10^{-5}$ kg/(m·s)
Coefficient of surface tension	$\sigma = 0.027$ kg/s^2
Density ratio	$\hat{\rho} = \rho_L/\rho_G = 15.6$
Viscosity ratio	$\hat{\mu} = \mu_L/\mu_G = 249.5$

TABLE 4: Description of computational cases studied including their respective non-dimensional quantities

Case ID	Fuel	Inlet diameter (D) (μm)	U_{inj} (m/s)	Density ratio $\frac{\rho_L}{\rho_G}$	Reynolds number $\frac{\rho_L U_{inj} D}{\mu_L}$	Weber number $\frac{\rho_L U_{inj}^2 D}{\sigma}$	Ohnesorge number $\frac{\sqrt{We_L}}{\mathrm{Re}_L}$
1	Isooctane	90	20	13.76	2.6×10^3	1.24×10^3	1.358×10^{-2}
2	Isooctane	90	30	13.76	3.9×10^3	2.79×10^3	1.358×10^{-2}
3	Isooctane	90	50	13.76	6.5×10^3	7.74×10^3	1.358×10^{-2}
4	Isooctane	30	30	13.76	1.3×10^3	0.93×10^3	2.353×10^{-2}
5	Isooctane	30	40	13.76	1.7×10^3	1.65×10^3	2.353×10^{-2}
6	Isooctane	30	50	13.76	2.2×10^3	2.58×10^3	2.353×10^{-2}
7	Isooctane	30	70	13.76	3.0×10^3	5.06×10^3	2.353×10^{-2}
8	Isooctane	30	50	20.8	2.2×10^3	2.58×10^3	2.353×10^{-2}
9	Isooctane	30	50	27.5	2.2×10^3	2.58×10^3	2.353×10^{-2}
10	JP-5	30	70	16	8.11×10^2	2.41×10^3	6.05×10^{-2}
11	HRD-76	30	70	15.6	2.50×10^2	2.17×10^3	1.86×10^{-1}

Due to the random nature (statistically stationary) of the various quantities computed, a temporal averaging procedure is employed to calculate the statistics, denoted by $(\langle \ldots \rangle)$. The initial point in the time integration corresponds to a time when the transient associated with the start of injection has passed, and the end point is chosen to ensure time-averaged convergence. The metrics employed in the current work correspond to planar flux integrated quantities as a function of distance from the injector nozzle [this is a metric that is often used to characterize sprays, e.g., Desantes et al. (2006); Payri et al. (2011)]. They are given by

$$\dot{m}_\Gamma(z,t) = \int_{A_z} \rho(\mathbf{x},t) U_z(\mathbf{x},t) \chi_\Gamma(\mathbf{x},t) dS, \tag{9}$$

$$\dot{m}_L(z,t) = \int_{A_z} \rho(\mathbf{x},t) U_z(\mathbf{x},t) \chi_L(\mathbf{x},t) dS, \tag{10}$$

where $U_z (= \mathbf{u}(\mathbf{x},t) \cdot \mathbf{e}_z)$ is the axial velocity, and the cross-sectional area perpendicular to the z-axis is denoted by A_z (cross-sectional area of entire domain). We refer to $\dot{m}_\Gamma(z,t)$ as an interfacial region mass flux. The indicator function used to isolate this interfacial region is denoted by $\chi_\Gamma(\mathbf{x},t)$ and it is defined at the computational cell level as

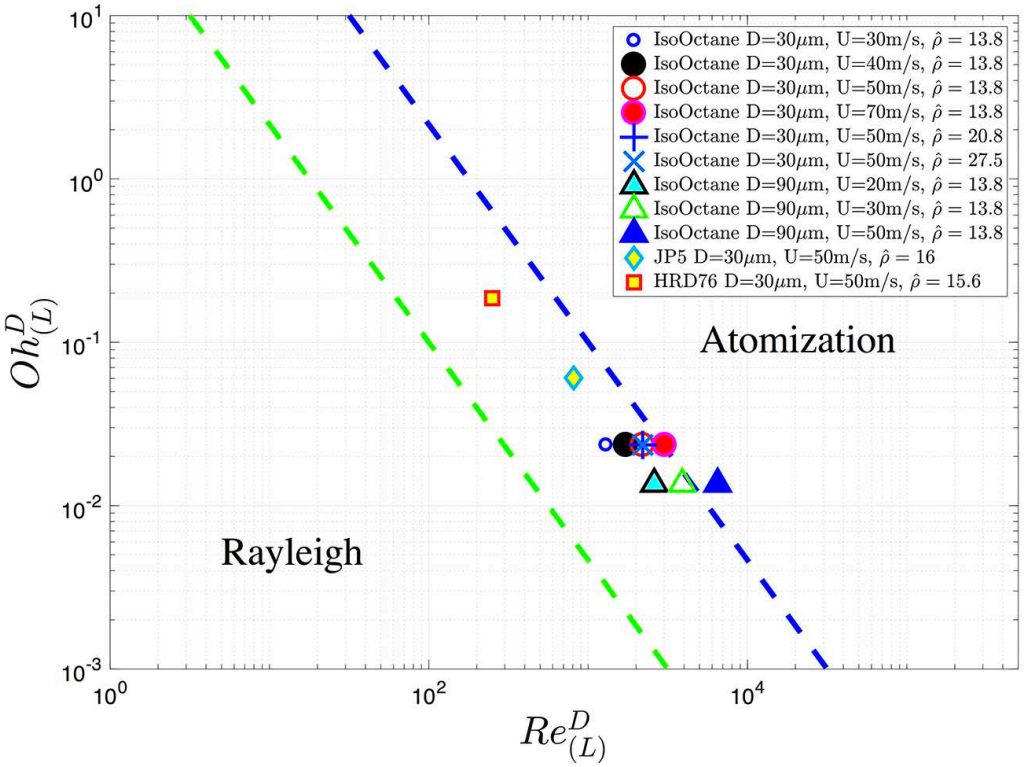

FIG. 2: Location of simulation cases (Table 4) within the atomization regime map of Reitz and Bracco (1986)

$$\chi_\Gamma(\mathbf{x},t) = \begin{cases} 1 & \text{if } 0.05 \leq \alpha(\mathbf{x},t) \leq 0.95 \text{ and the associated cell} \\ & \text{is topologically connected to the } \alpha(\mathbf{x},t) > 0.95 \text{ region.} \\ 0 & \text{otherwise.} \end{cases} \tag{11}$$

This indicator function is updated throughout the domain every $10\Delta t$ for the $D = 90$ μm cases, and every 20–$25\Delta t$ for the 30 μm cases. In an algebraic VoF scheme, such as the one present in InterFoam, this methodology of computing $\dot{m}_\Gamma(z,t)$ offers an attractive procedure by which to gauge the extent of the interfacial region. In a similar fashion, the indicator function, $\chi_L(\mathbf{x},t)$, is employed to identify the liquid region of the domain, i.e. $\alpha(\mathbf{x},t) > 0.95$.

To track the downstream growth of the interfacial region as a result of atomization, the following ratio is employed:

$$\Phi_m(z) \equiv \left\langle \frac{\dot{m}_\Gamma(z,t)}{\dot{m}_L(z,t)} \right\rangle . \tag{12}$$

This quantity will be denoted as the normalized interfacial mass flow rate. Again, the brackets $\langle \ldots \rangle$ denote converged temporal averages.

Since interfacial momentum transfer is a key parameter investigated in the present work, the phasic velocities are also extracted from the simulations. These quantities are obtained from

$$\langle \overline{U}_{z,q}(z_p,t)\rangle \equiv \left\langle \frac{\int_{CV_p} U_z(\mathbf{x},t)\chi_q(\mathbf{x},t)dV}{\int_{CV_p}\chi_q(\mathbf{x},t)dV}\right\rangle, \tag{13}$$

where $q \in (L,G)$. The velocities are integrated over control volumes, CV_p, to provide us with slightly more global quantities than velocities defined at the computational cell level. The length of each control volume ranges between 5 and 6.66 diameters in the streamwise direction, and their traverse and spanwise extent are 7 diameters, respectively. The centers of all CV_p lie along the jet axis. These velocity metrics are used to gauge the momentum interaction between the liquid and gas phases in the subsequent results. In shorthand, they are simply referred by $\langle \overline{U}_z\rangle$, where the corresponding phase will be indicated in the respective plots.

3.1 Resolution Concerns

It is expected that at some point during the breakup process, a fraction of the smallest liquid structures will be at or below the level of grid resolution. In the present algebraic VoF scheme, liquid mass is well conserved; however, the shape representation of objects having a size less than approximately $4\Delta x$ suffers significantly. These inadequately resolved objects can be identified by observing that throughout their physical domain, the liquid fraction of the associated cells is well below one.

To quantify the degree of unresolved liquid present in the simulations, the following normalized flux is employed:

$$\tilde{\dot{m}}_{unr}(z,t) \equiv \frac{\dot{m}_{(unr}(z,t)}{\dot{m}_L(0,t)}, \tag{14}$$

where

$$\dot{m}_{unr}(z,t) = \int_{A_z} \rho(\mathbf{x},t)U_z(\mathbf{x},t)\chi_{unr}(\mathbf{x},t)dS, \quad \text{and} \tag{15}$$

$$\dot{m}_L(0,t) = \int_{A_{nozzle}} \rho_L U_z(\mathbf{x},t)dS. \tag{16}$$

Here $\chi_{unr}(\mathbf{x},t)$ is the corresponding indicator function for the unresolved regions of the two-phase flow. Analogous to the interfacial mass fluxes defined previously, $\dot{m}_{unr}(z,t)$ tracks the amount of unresolved liquid across a given plane, A_z, located at an arbitrary distance, z, from the nozzle exit. The normalization factor is the total mass flux of liquid being injected into the system, which is simply a mass flux integral over the nozzle area (A_{nozzle}). Profiles for $\tilde{\dot{m}}_{unr}$ are shown in Fig. 3 for case 6 (Table 4), corresponding to different levels of resolution beginning with $\Delta x = 2.5$ μm and ending at $\Delta x = 1.5$ μm. Results for $D/\Delta x = 12$ or $\Delta x = 2.5$ μm, show that while initially, the degree of inadequately resolved liquid is relatively small, once the jet undergoes complete breakup, $\tilde{\dot{m}}_{unr}$ rises to unacceptable levels. At $\Delta x = 1.875$ μm, the maximum value for $\tilde{\dot{m}}_{unr}$ is approximately 15%, and at $\Delta x = 1.5$ μm, that value is reduced to 10%. For all calculations presented for the $D = 30$ μm cases, a value of $\Delta x = 1.875$ μm is used in the refined regions, with the exception of case 7 (U_{inj} =70 m/s), where a finer resolution of $\Delta x = 1.5$ μm is required. With respect to the $D = 90$ μm cases, this level of resolution is excessive; hence, $\Delta x = 3.75$ μm is used. For these larger diameter cases, results for Φ_m are only presented where $\tilde{\dot{m}}_{unr}$ is reasonably low.

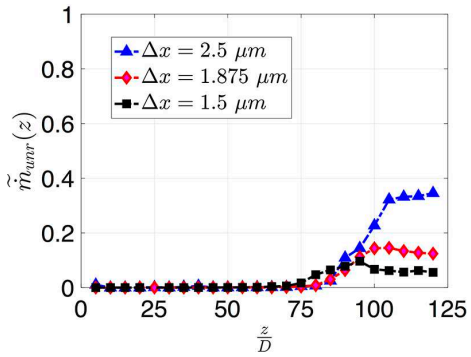

FIG. 3: Unresolved liquid mass flux as a function of grid resolution for case # 6 ($D = 30$ μm and $U_{inj} = 50$ m/s)

4. RESULTS

We begin with a visualization of typical results, which are displayed in Fig. 4. These correspond to the 90 μm isooctane cases, and the images show the interface colored by velocity magnitude. As liquid breaks off from the jet surface and travels radially outward, its corresponding velocity decreases as a result of continuous interaction with the surrounding quiescent gas. Hence, the higher moving liquid bodies are concentrated in the center of the jet analogous to single-phase jets.

In all three cases shown in Fig. 4, the region closest to the nozzle is characterized by a fairly intact liquid structure with a few surrounding droplets. We will refer to this region as the near-field. Moving downstream from this region, we find the location where primary atomization occurs. This region is characterized by the complete fragmentation of the liquid jet. At 20 m/s, the fragmentation of the jet is easily distinguishable since the surrounding droplet field is relatively sparse. At 30 m/s, the primary atomization section has become somewhat obscured, and at 50 m/s, the details of the intact liquid core are hardly discernible. This is, in fact, the problem encountered by many diagnostic techniques aimed at resolving the internal details of the liquid core breakup (Kastengren et al., 2014; Linne et al., 2006), particularly at high-speed injection conditions, such as those pertaining to diesel engines ($\sim$ 500 m/s). The normalized interfacial mass flow rates corresponding to the images shown in Fig. 4 are plotted together in Fig. 5. Initially, the liquid jet remains fairly intact for approximately 30 diameters from the nozzle with a few droplets in this part of the domain as shown in Fig. 4. Around $z/D = 30$, the interfacial area grows rapidly as a result of primary atomization. This is reflected by a noticeable change in the slope of the $\Phi_m(z)$ profiles. For the 20 m/s case, this change in slope is relatively mild, since the creation of the interfacial area is relatively small. At 50 m/s, however, the change in slope is significantly more pronounced as a direct consequence of the more vigorous atomization (see Fig. 4). Depending on the injection velocity and the associated Weber number, the $\Phi_m(z)$ curves eventually reach a peak somewhere between $z/D = 60$ and $z/D = 80$. Beyond this point, there is a slight decrease in $\Phi_m(z)$, which is caused by coalescence and deceleration of the liquid. For the 50 m/s case, the results are only plotted up to $z/D = 60$. Beyond this point the amount of unresolved liquid is excessive, and the predictions are not reliable.

For the $D = 30$ μm isooctane cases, the interfacial mass flux profiles are shown in Fig. 6, and the results display a similar trend as the one depicted for the larger diameter calculations,

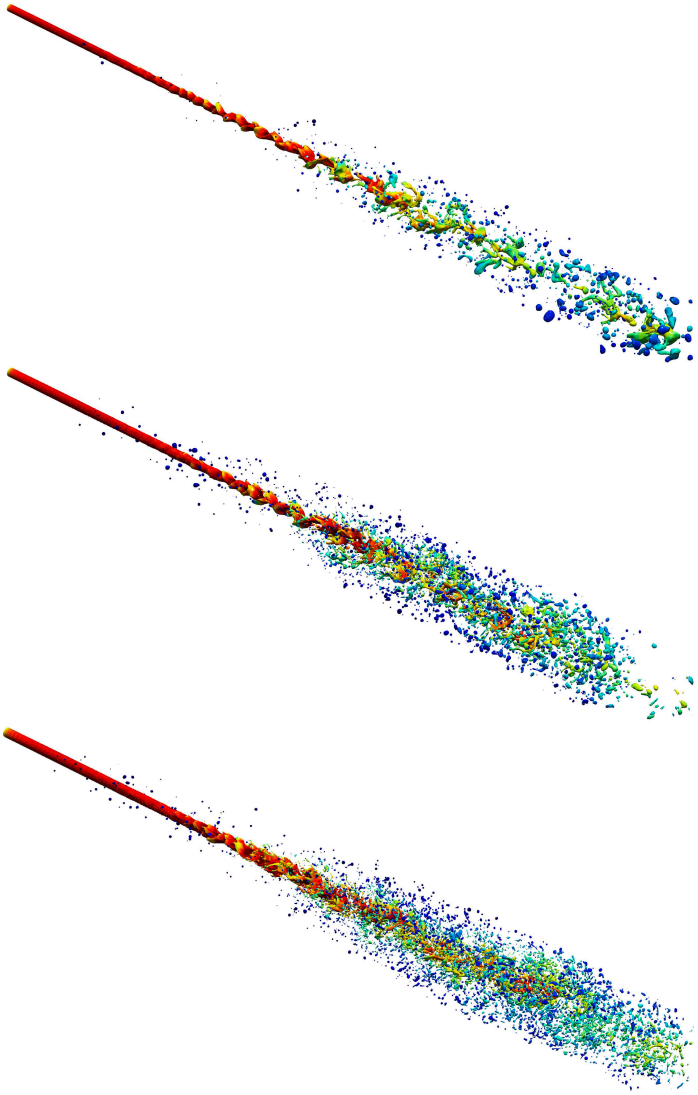

FIG. 4: Liquid jet atomization corresponding to the $D = 90$ μm isooctane cases, where $U_{inj} = 20$, 30, and 50 m/s from the top to the bottom, respectively. The interface is colored by velocity magnitude where red corresponds to U_{inj} and dark blue corresponds to zero velocity

albeit at smaller values. The $\Phi_m(z)$ curves show a steepening profile with increasing injection velocity. At lower velocities, $\Phi_m(z)$ reaches an asymptotic value at approximately 150 diameters downstream. For the higher injection cases, a reduction in $\Phi_m(z)$ is observed beyond the peak value. This is due both to a diminishing presence of interfacial area, as liquid structures coalesce, but also is a result of liquid deceleration, as discussed previously.

In Figs. 7, 8, and 9, respectively for cases 1, 2, and 3, respectively, the $\Phi_m(z)$ curves are examined together with their respective phasic velocity profiles. Considering case 1 shown in Fig. 7, it becomes clear that the $\Phi_m(z)$ profile can be characterized by three distinct regimes as

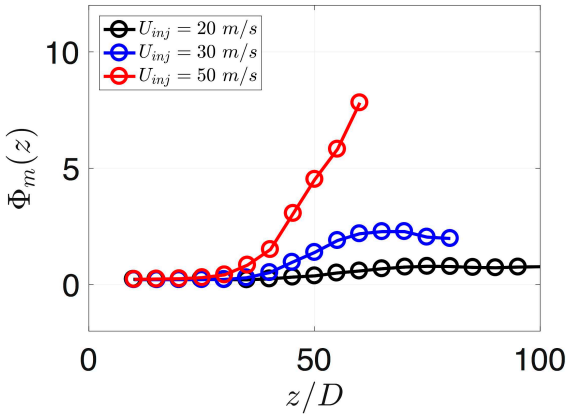

FIG. 5: Normalized interfacial mass flow rate profiles, $\Phi_m(z)$, corresponding to the $D = 90$ μm isooctane cases

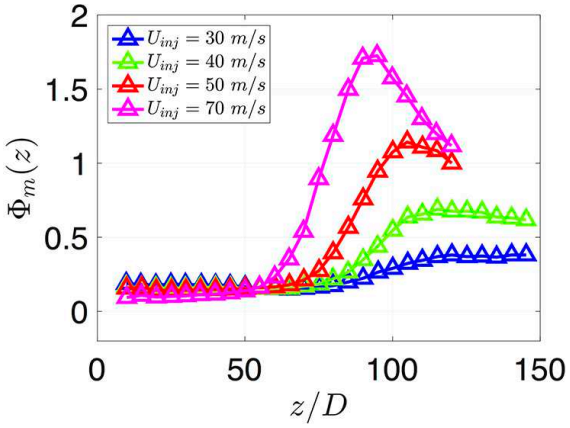

FIG. 6: Normalized interfacial mass flow rate profiles, $\Phi_m(z)$, corresponding to the $D = 30$ μm isooctane cases

indicated by the superimposed lines on the plot. The first regime depicts a preliminary state of the jet, where the liquid core is fairly intact with only some minor perturbations on its surface. This domain extends from $z/D = 0$ to approximately $z/D = 30$. A few droplets exist in this domain, but they are mostly the remnants of the start of injection. The associated phasic velocity profiles in this region begin with the assigned injection velocity at $z/D = 0$ for the liquid and the zero ambient velocity for the gas phase (noting again that the liquid at the nozzle exit has a flat hat profile). As we progress downstream, a mild deceleration in the liquid is observed with a likewise mild acceleration of the gas phase. This indicates that the momentum coupling between the phases is taking place but that it is relatively weak.

In the atomization region, which is located in the range $30 \lesssim z/D \lesssim 70$ for case 1, a change in the slope of $\Phi_m(z)$ is observed. The associated phasic velocities also reflect a more pronounced difference, since in this part of the domain the interfacial area is growing, leading to better momentum exchange between the liquid and gas phase regions. Beyond the atomization

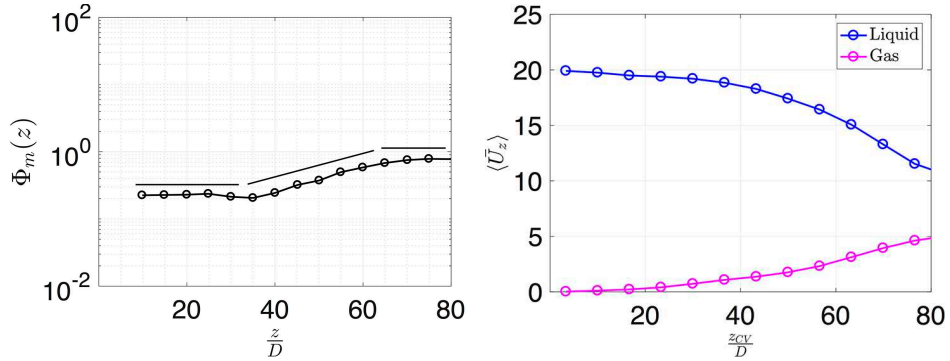

FIG. 7: Φ_m and phasic mean velocities corresponding to $D = 90$ μm and $U_{inj} = 20$ m/s (isooctane)

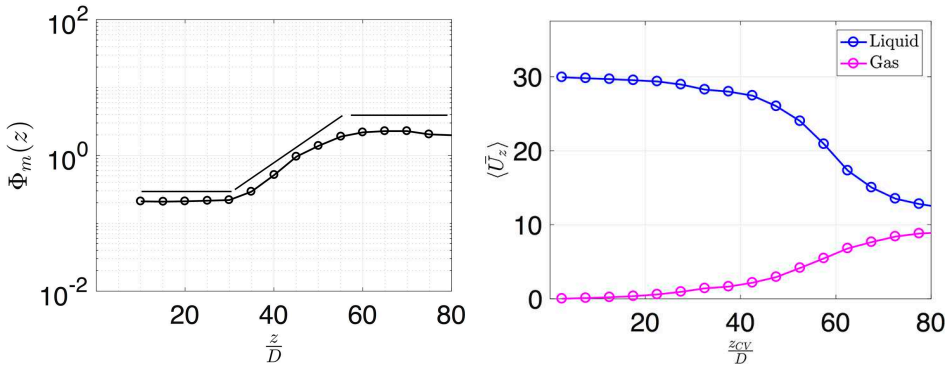

FIG. 8: Φ_m and phasic mean velocities corresponding to $D = 90$ μm and $U_{inj} = 30$ m/s (isooctane)

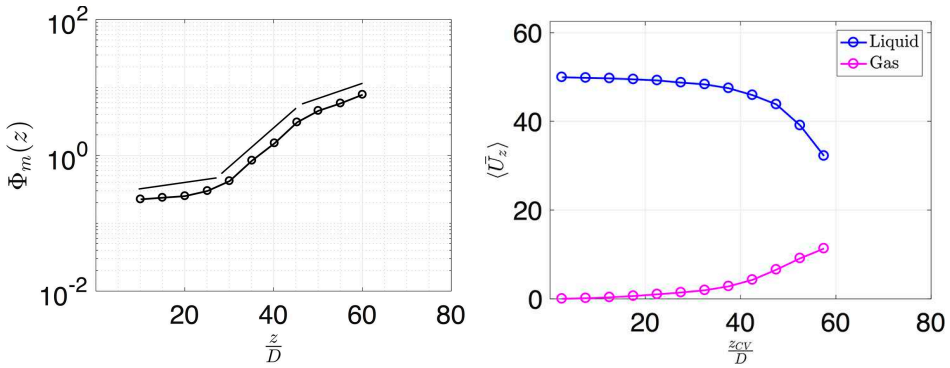

FIG. 9: Φ_m and phasic mean velocities corresponding to $D = 90$ μm and $U_{inj} = 50$ m/s (isooctane)

region – that is, for $z/D \gtrsim 70$ for case 1, – breakup has mostly ceased, and the difference between phasic velocities has shrunk to approximately 7–9 m/s and continues to decrease with increasing distance from the nozzle.

For the 30 and 50 m/s cases shown respectively in Figs. 8 and 9, the results are qualitatively similar to the slower 20 m/s case, with the main difference being that the $\Phi_m(z)$ and phasic velocity profiles have more pronounced slopes for the higher velocity cases. Additionally, at the

higher injection speeds, the results show that the degree of phasic velocity convergence towards a unique value appears much more evident than for the lower injection cases. At these higher injection velocities, the interfacial area growth is more significant, thereby facilitating a more vigorous momentum exchange. Also at the higher speeds, the distinction between the initial region and the middle atomization region begins to blur; that is, the change in slope for $\phi_m(z)$ is not as distinct as in Fig. 7.

For the $D = 30$ μm isooctane cases, the results for $\Phi_m(z)$ and $\langle \overline{U}_z \rangle$ are shown in Figs. 10, 11, 12, and 13. Again, in a similar fashion to the $D = 90$ μm cases, the three regimes during the spray formation process can be identified in these plots, with their presence becoming more pronounced with increasing injection velocity. Also, the liquid velocity profiles are initially flat but are not equal to U_{inj} since the velocity profile is no longer assigned a uniform value at the nozzle exit. As primary atomization unfolds and both phases exchange momentum, substantial variations in the velocity profiles are observed. This is followed by an approach towards equilibrium between both phases as their respective velocities asymptotically approach a unique value. Key differences between these smaller diameter cases and the 90 μm computations are that the distinctiveness of the spray regimes remains sharp even at 70 m/s. Also, the ability to computationally resolve more of the spray for the smaller diameter cases allows us to capture more of the asymptotic equilibrium state, which shows more compellingly the asymptotic convergence of the velocity fields, particularly at 70 m/s.

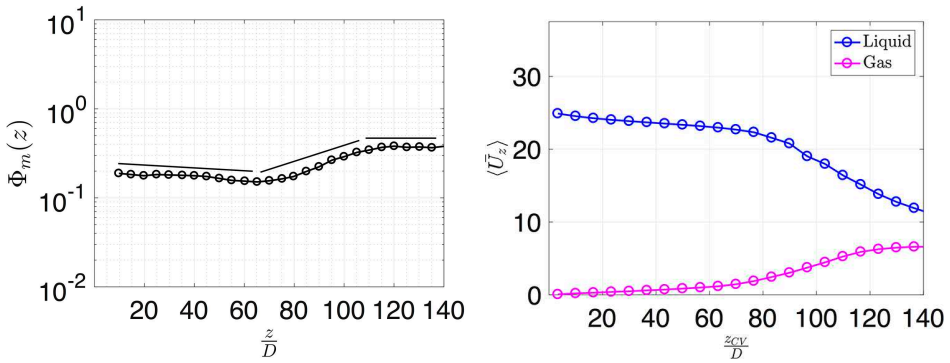

FIG. 10: Φ_m and phasic mean velocities corresponding to $D = 30$ μm and $U_{inj} = 30$ m/s (isooctane)

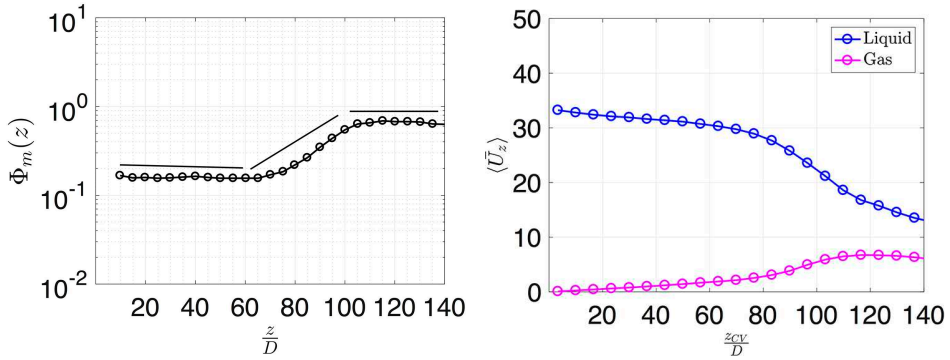

FIG. 11: Φ_m and phasic mean velocities corresponding to $D = 30$ μm and $U_{inj} = 40$ m/s (isooctane)

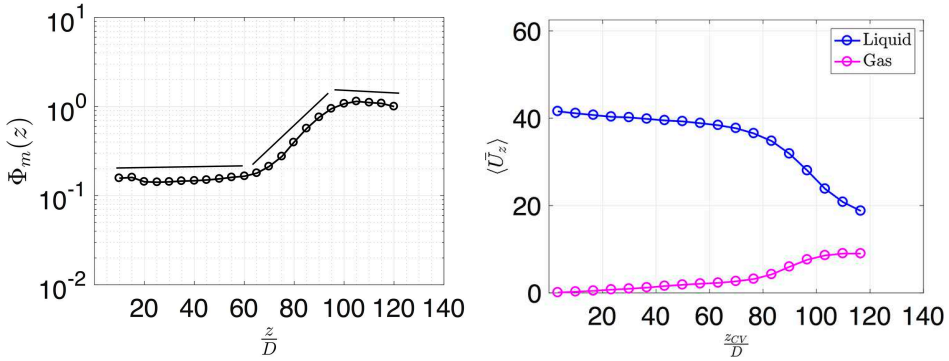

FIG. 12: Φ_m and phasic mean velocities corresponding to $D = 30$ μm and $U_{inj} = 50$ m/s (isooctane)

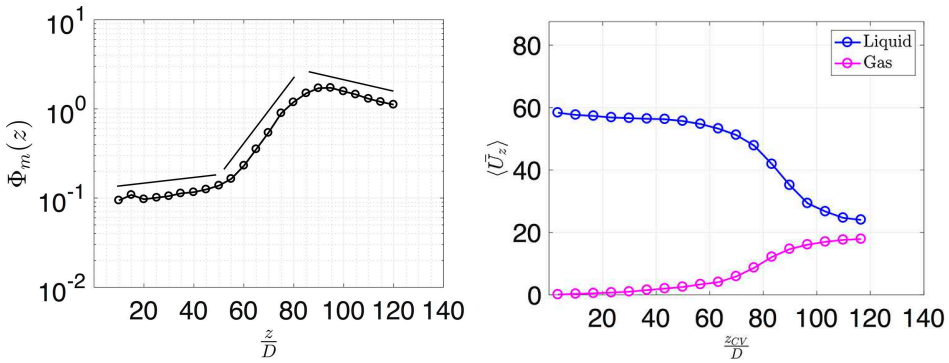

FIG. 13: Φ_m and phasic mean velocities corresponding to $D = 30$ μm and $U_{inj} = 70$ m/s (isooctane)

4.1 Results for Different Fluids and Conditions

Additional spray cases are reported in this section for isooctane under different ambient density conditions, as well as jet fuel, JP-5, and a hydroprocessed naval renewable fuel, HRD-76. These cases are documented in Table 4, cases 8 through 11. For the isooctane cases at milder density ratios, namely $\hat{\rho} = 20.8$ and $\hat{\rho} = 27.5$, the results shown in Figs. 14 and 15 reflect the clear distinction between the three regimes discussed previously. The only noticeable change is the lengthening of the intact liquid core with increasing density ratio, which is an effect that has been experimentally reported in the work of Faeth et al. (1995). By shifting the atomization regime further downstream, the intensity of the momentum exchange between the phases is also displaced, resulting in a relatively smaller degree of momentum equilibration over the entire domain. Specifically, the pronounced downward and upward trend of the mean liquid and gas velocities, respectively, occurs at larger distances from the nozzle as the density ratio increases.

With respect to the different fuels, the non-dimensional quantities pertaining to JP-5, as seen in Fig. 16, are in the same neighborhood as the lower velocity $D = 30$ μm isooctane cases. This gives interfacial mass flow rates and phasic velocity profiles that are naturally similar to those isooctane cases. However, for HRD-76, as shown in Fig. 17, the Reynolds number is approximately a factor of 5 times smaller than the mildest isooctane case (case 4). The result is a noticeably minor degree of atomization, where the liquid structures produced by the breakup are of the same length scale as the jet. Consequently, the $\Phi_m(z)$ profile for HRD-76 barely shows

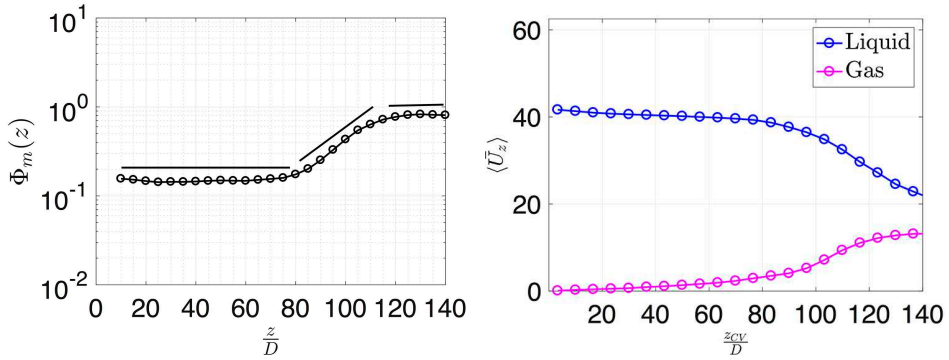

FIG. 14: Φ_m and phasic mean velocities corresponding to isooctane at $D = 30$ µm, $U_{inj} = 50$ m/s, and $\hat{\rho} = 20.8$

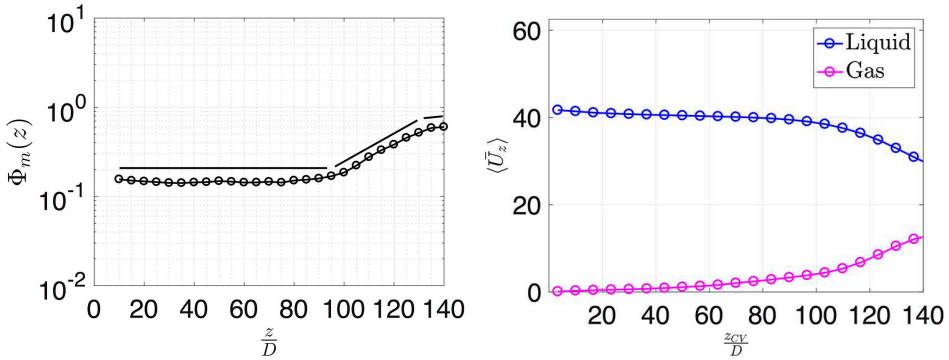

FIG. 15: Φ_m and phasic mean velocities corresponding to isooctane at $D = 30$ µm, $U_{inj} = 50$ m/s, and $\hat{\rho} = 27.5$

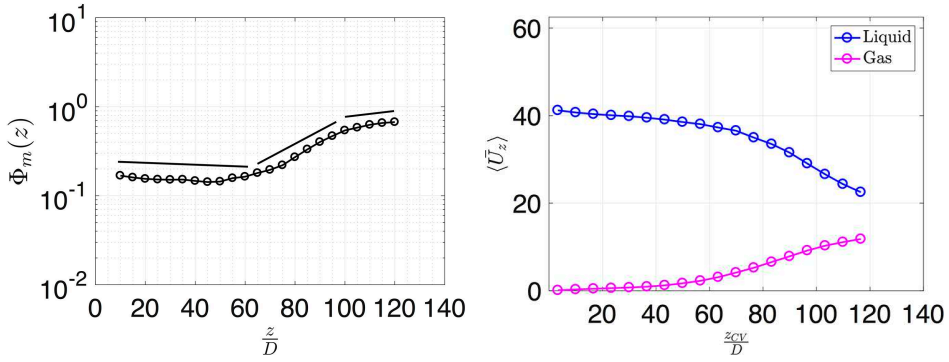

FIG. 16: Φ_m and phasic mean velocities corresponding to JP-5 at $D = 30$ µm, $U_{inj} = 70$ m/s, and $\hat{\rho} = 16$

the presence of the three regimes, and the phasic velocity profiles do not exhibit the typical pronounced shape in the atomization regime observed for higher Re cases.

To examine more closely the phasic velocity behavior, radial profiles at different axial locations are presented in Fig. 18 corresponding to case 6 conditions. The radial and axial extent of each of these bins is $\Delta r = 1.5$D and $\Delta z = 5$D, respectively. The results show that relatively

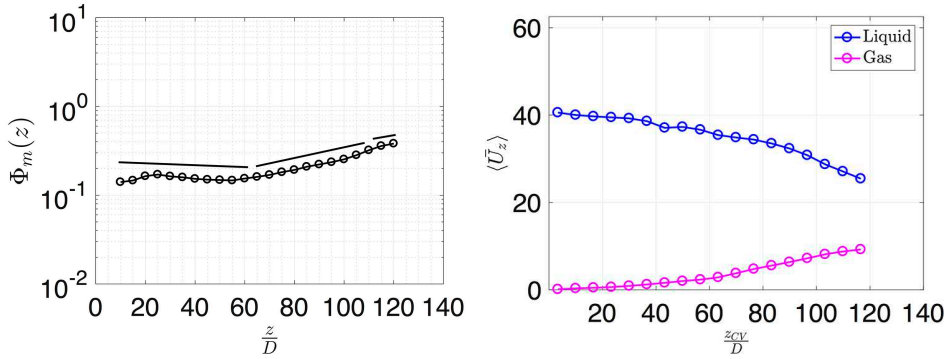

FIG. 17: Φ_m and phasic mean velocities corresponding to HRD-76 at $D = 30$ μm, $U_{inj} = 70$ m/s, and $\hat{\rho} = 15.6$

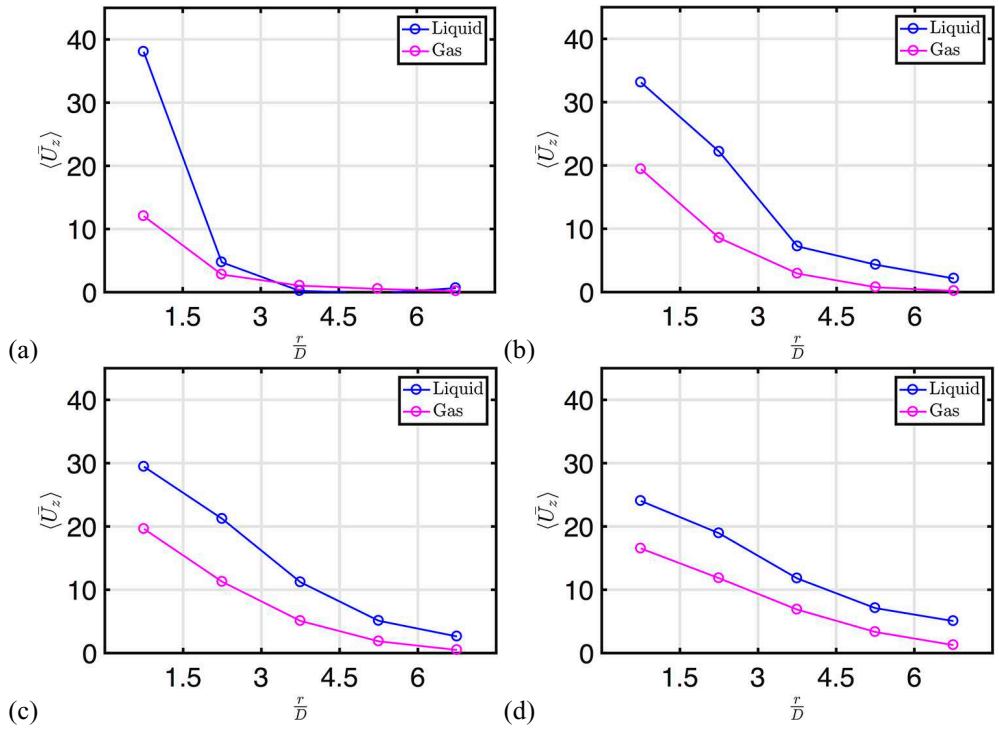

FIG. 18: Radial velocity profiles of phasic velocities at (a) $z/D \in [70, 75]$, (b) $z/D \in [90, 95]$, (c) $z/D \in [100, 105]$, and (d) $z/D \in [115, 120]$ for isooctane $D = 30$ μm and $U_{inj} = 50$ m/s

close to the nozzle exit ($z/D \in [70, 75]$), the liquid velocity is relatively high and concentrated around the centerline of the spray. The gas velocity distribution in this part of the domain is also localized around the center, but it has much lower value than the liquid. Downstream of this location both phasic profiles display the effect of diffusion as the profiles become more radially broad. Also, the effect of interphase momentum brings the profiles closer to each other as we move downstream. For instance, at $z/D \in [115, 120]$, the overall velocity difference has been reduced to approximately 5 m/s.

4.2 Analysis

A simplified mathematical model (conveniently named toy model in the physics literature) can be developed to reduce the complexity of the jet breakup process to its most dominant physics. The hope here is that these analytical solutions will provide insight into the trends shown in the previous section. In this spirit, we begin with momentum conservation for the liquid and gas phase *material* regions (Ω_L and Ω_G, respectively), namely

$$\rho_L \frac{D}{Dt}\int_{\Omega_L} \mathbf{u} dV = \int_{\partial\Omega_L} \boldsymbol{\sigma}_L \cdot \mathbf{n}_L dS + \rho_L \int_{\Omega_L} \mathbf{g} dV, \tag{17}$$

and

$$\rho_G \frac{D}{Dt}\int_{\Omega_G} \mathbf{u} dV = \int_{\partial\Omega_G} \boldsymbol{\sigma}_G \cdot \mathbf{n}_G dS + \rho_G \int_{\Omega_G} \mathbf{g} dV. \tag{18}$$

Here $\mathbf{n}_L$ and $\mathbf{n}_G$, and $\boldsymbol{\sigma}_L$ and $\boldsymbol{\sigma}_G$ are the respective unit outward normal vectors (from Ω) and stress tensors for the liquid and gas phases. These material regions reflect in a representative manner the liquid body associated with the jet and the gas phase region that interacts with this liquid body. Assuming constant fluid properties, the left-hand-side (LHS) terms in Eqs. (17) and (18) represent the rate of momentum change in balance with the surface and body forces of the right-hand-side (RHS).

Considering the fact that the Froude numbers are much greater than one and that the relevant time period is $\mathcal{O}(10^{-3})$ s in the present simulations, we can safely ignore the gravitational contributions. Additionally, it can be assumed that the most significant contributions to momentum change for each phase is through the interaction with the other phase, and this is taking place through the interface, Γ. Furthermore, we can rewrite the LHS terms using the mean value theorem to denote liquid and gas phase averages, namely $\overline{\mathbf{u}}_L$ and $\overline{\mathbf{u}}_G$. This yields

$$\rho_L |\Omega_L| \frac{d\bar{\mathbf{U}}_L}{dt} = \int_\Gamma \boldsymbol{\sigma}_L \cdot \mathbf{n}_L dS, \tag{19}$$

and

$$\rho_G |\Omega_G| \frac{d\bar{\mathbf{U}}_G}{dt} = \int_\Gamma \boldsymbol{\sigma}_G \cdot \mathbf{n}_G dS. \tag{20}$$

Here, we have used $D|\Omega_{L,G}|/Dt = 0$ from the incompressibility constraint. These vector equations can be projected along streamwise unit vector, $\mathbf{e}_z$, to arrive at a balance in the direction of injection, namely

$$\rho_L |\Omega_L| \frac{d\bar{U}_L}{dt} = \int_\Gamma (\boldsymbol{\sigma}_L \cdot \mathbf{n}_L) \cdot \mathbf{e}_z \, dS = F_L, \tag{21}$$

and

$$\rho_G |\Omega_G| \frac{d\bar{U}_G}{dt} = \int_\Gamma (\boldsymbol{\sigma}_G \cdot \mathbf{n}_G) \cdot \mathbf{e}_z \, dS = F_G. \tag{22}$$

The solution to Eqs. (21) and (22) require instantaneous knowledge of the local traction at each point in Γ and as a function of time. In an effort to arrive at an approximate closed-form relationship, these traction forms are approximated by

$$\int_\Gamma (\boldsymbol{\sigma}_L \cdot \mathbf{n}_L) \cdot \mathbf{e}_z dS = F_L = K_L(\bar{U}_G - \bar{U}_L)A_\Gamma, \tag{23a}$$

$$\int_{\Gamma}(\boldsymbol{\sigma}_G \cdot \mathbf{n}_G)\cdot \mathbf{e}_z dS = F_G = K_G(\bar{U}_L - \bar{U}_G)A_\Gamma, \tag{23b}$$

where A_Γ is the interfacial area. This approximation is motivated by an empirical treatment stemming from the form taken by drag coefficients, for example, Prosperetti and Tryggvason (2009),

$$C_D = \frac{F_{L,z}}{1/2\rho_G A|\bar{U}_L - \bar{U}_G|^2}, \tag{24}$$

where A is the projected area of the liquid body in the z-direction. In the approximations above [Eqs. (23a,b)], we have essentially retained only the Re_r^{-1} term in the drag coefficient expression, where $\mathrm{Re}_r = \Lambda_L|\bar{U}_L - \bar{U}_G|/\mu_G$, and Λ_L is the associated length scale of the liquid body. In doing so, we understand that this approximation is limited at relatively large values of Re_r, but becomes better as the phasic velocities converge towards their respective equilibrium value.

Since there are no external forces being applied to the two-phase system, it is expected that the rate of change for total momentum is zero. This directly implies that the traction terms in the RHS of Eqs. (21) and (22) are equal and opposite. Furthermore, it implies that the traction does not suffer a jump across the interface. With the relatively large values for the Weber numbers considered (Table 4), neglecting the jump in the interfacial traction is a good approximation. This leads to $K_L = K_G = K$ and transforms Eqs. (21), (22), and (23), into

$$\frac{d\bar{U}_z^L}{dt} = \frac{K}{\rho_L|\Omega_L|}(\bar{U}_z^G - \bar{U}_z^L)A_\Gamma = \frac{1}{\tau_L}(\bar{U}_z^G - \bar{U}_z^L), \tag{25a}$$

$$\frac{d\bar{U}_z^G}{dt} = \frac{K}{\rho_G|\Omega_G|}(\bar{U}_z^L - \bar{U}_z^G)A_\Gamma = \frac{1}{\tau_G}(\bar{U}_z^L - \bar{U}_z^G), \tag{25b}$$

where the time constants, τ_L and τ_G are respectively equal to $(\rho_L|\Omega_L|)/(KA_\Gamma)$ and $(\rho_G|\Omega_G|)/(KA_\Gamma)$. These equations can be expressed in compact form as

$$\begin{bmatrix} d\bar{U}_L/dt \\ d\bar{U}_G/dt \end{bmatrix} = \begin{bmatrix} -1/\tau_L & 1/\tau_L \\ 1/\tau_G & -1/\tau_G \end{bmatrix} \begin{bmatrix} \bar{U}_L \\ \bar{U}_G \end{bmatrix}, \tag{26}$$

resulting in the following closed-form solution for the phasic velocities:

$$\begin{bmatrix} \bar{U}_L(t) \\ \bar{U}_G(t) \end{bmatrix} = C_1 \begin{bmatrix} 1/\sqrt{2} \\ 1/\sqrt{2} \end{bmatrix} + C_2 \begin{bmatrix} \tau_G/\sqrt{\tau_L^2+\tau_G^2} \\ -\tau_L/\sqrt{\tau_L^2+\tau_G^2} \end{bmatrix} \exp\left[-\left(\frac{1}{\tau_G}+\frac{1}{\tau_L}\right)t\right]. \tag{27}$$

This expression can be rewritten as

$$\begin{aligned} \begin{bmatrix} \bar{U}_L(t) \\ \bar{U}_G(t) \end{bmatrix} &= C_1 \begin{bmatrix} 1/\sqrt{2} \\ 1/\sqrt{2} \end{bmatrix} \\ &+ \frac{C_2}{\sqrt{(\rho_L\Omega_L)^2+(\rho_G\Omega_G)^2}} \begin{bmatrix} +\rho_G\Omega_G \\ -\rho_L\Omega_L \end{bmatrix} \exp\left[-A_\Gamma K\left(\frac{1}{\rho_G\Omega_G}+\frac{1}{\rho_L\Omega_L}\right)t\right]. \end{aligned} \tag{28}$$

The constants C_1 and C_2 can be obtained from the following initial conditions:

$$\bar{U}_L(0) = \frac{C_1}{\sqrt{2}} + \frac{C_2\rho_G\Omega_G}{\sqrt{(\rho_L\Omega_L)^2+(\rho_G\Omega_G)^2}} = U_{inj}, \tag{29}$$

for the liquid phase, and

$$\bar{U}_G(0) = \frac{C_1}{\sqrt{2}} - \frac{C_2 \rho_L \Omega_L}{\sqrt{(\rho_L \Omega_L)^2 + (\rho_G \Omega_G)^2}} = 0, \tag{30}$$

for the gas phase. Both of these equations can be used to solve for constants C_1 and C_2, resulting in the final form for the phasic velocities, namely

$$\bar{U}_L(t) = \frac{U_{inj}}{\rho_L \Omega_L + \rho_G \Omega_G} \left[\rho_L \Omega_L + \rho_G \Omega_G \exp\left(-A_\Gamma K \left[\frac{1}{\rho_G \Omega_G} + \frac{1}{\rho_L \Omega_L} \right] t \right) \right], \tag{31}$$

and

$$\bar{U}_G(t) = \frac{U_{inj}}{\rho_L \Omega_L + \rho_G \Omega_G} \left[\rho_L \Omega_L - \rho_L \Omega_L \exp\left(-A_\Gamma K \left[\frac{1}{\rho_G \Omega_G} + \frac{1}{\rho_L \Omega_L} \right] t \right) \right]. \tag{32}$$

Although $\rho_L \gg \rho_G$, Ω_L is typically significantly smaller than Ω_G, and thus we cannot directly dismiss $\rho_G \Omega_G$ in favor $\rho_L \Omega_L$. Both of these quantities remain in the above expressions. At initial times, the interfacial area, which for the sake of the model we are treating as constant, is relatively small. This means that the argument in the exponential remains minute, indicating a very mild change in $\bar{U}_L(t)$ and $\bar{U}_G(t)$. This corresponds to the first regime in the spray development process indicated above in the liquid injection calculations for various plots of $\Phi_m(z)$ and phasic velocities. This regime pertains to the initial destabilization of the liquid jet, where the momentum coupling between both phases is weak. As we proceed into the atomization region, Γ grows significantly due to aerodynamic breakup. Mathematically, this makes the argument in the exponential in Eqs. (31) and (32) much greater than in the previous regime, forcing a substantial change in the phasic velocities. Referring to Figs. 7 through 13, a large change in these velocities is similarly captured in the simulations.

Finally, for sufficiently large times, both $\bar{U}_L(t)$ and $\bar{U}_G(t)$ approach a unique value given by

$$\lim_{t\to\infty} \bar{U}_L(t) = \lim_{t\to\infty} \bar{U}_G(t) = \frac{U_{inj} \rho_L \Omega_L}{\rho_L \Omega_L + \rho_G \Omega_G}. \tag{33}$$

This corresponds to the dynamic equilibrium state in the third regime, and it represents the end state of the momentum exchange process between the liquid and gas phase. Note that as $\rho_L \Omega_L$ increases, this limiting equilibrium velocity approaches U_{inj}, and only if the gas inertia is negligible does it become equal to U_{inj}. Under realistic conditions and considering the turbulence structures generated in these higher Re flows, this equilibrium is never truly reached. The magnitudes of $|\bar{U}_L - \bar{U}_G|$ are never zero, although they are significantly smaller than in the near-field region (Deshpande et al., 2011), and their decay is a direct function of the droplet time constant (Trujillo and Parkhill, 2011).

5. CONCLUSIONS

Two-phase flow simulations based on a VoF methodology are used to study the injection of a liquid jet into a quiescent gaseous environment. Our study focuses on the spray formation characteristics ranging from 0 to $\mathcal{O}(100)$ diameters downstream and considers the quasi-steady period, beyond the initial injection transient. For the range of velocities considered and associated non-dimensional quantities (Table 4), the spray is found to consist of three regimes:

1. The first regime (near-field) corresponds to the development of initial instabilities and subsequent surface fragmentation of the jet with the interior of the jet remaining intact. The momentum coupling between phases is relatively weak with the phasic average velocities displaying nearly flat profiles as a function of the streamwise coordinate.

2. In the second regime (mid-field), the jet core undergoes fragmentation producing a significant amount of interfacial area. This is the primary atomization stage. Consequently, a tremendous increase in momentum coupling between both phases is observed, resulting in large changes in the velocity development as we move downstream.

3. Beyond the breakup zone (far-field), an equilibration between both phases characterizes the third regime. A closed-form expression for an asymptotic equilibrium velocity is derived, which is given by $(U_{inj}\rho_L\Omega_L)/(\rho_L\Omega_L + \rho_G\Omega_G)$. The mean slip velocity between phases is relatively small in this part of the domain, thereby weakening the action of shear considerably as a driver for atomization. Consequently, the liquid mass and interfacial mass flow rates are again nearly flat, as is the case in the first region.

The three regions are pictorially summarized in Fig. 19.

It is observed that as the liquid-based Weber and Reynolds numbers increase, there is a shift from a clear three-regime characterization of the phasic velocities and interfacial mass flow rates to more gradually changing profiles with distance downstream from the nozzle. This is particularly evident for the 90 μm isooctane case at 50 m/s. Under these conditions, there is a significant creation of interfacial area in the near-field in contrast to the lower Weber conditions. Thus the rate of interfacial area creation (slope of $\Phi_m(z)$ curve) in the near-field begins to match the corresponding rate in the primary atomization region. It can be conjectured that for even larger Weber number cases, the primary atomization region ceases to be distinguished from the near-field. In the other extreme, for very mild cases of injection such as HRD-76, the three-regime identification is barely noticeable, since the atomization process is so weak that the $\Phi_m(z)$ curve hardly changes from the near- to the far-field.

ACKNOWLEDGMENTS

The authors would like to gratefully acknowledge the support from Caterpillar Corporation and the National Science Foundation through Grant No. 1703825. We are also thankful to the Advanced Computing Initiative at UW-Madison for providing computational resources, as well as to CEI for granting use of their post processing software, EnSight. Additionally, this work partially used the Extreme Science and Engineering Discovery Environment (XSEDE) Bridges regular memory at the Pittsburgh Supercomputing Center through allocation TG-CTS180037.

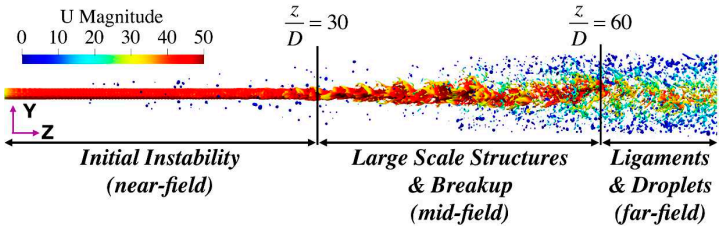

FIG. 19: The three regimes in the spray formation process. Interface is colored by velocity magnitude (U)

REFERENCES

Aulisa, E., Manservisi, S., and Scardovelli, R., A Mixed Markers and Volume-of-Fluid Method for the Reconstruction and Advection of Interfaces in Two-Phase and Free-Boundary Flows, *J. Comput. Phys.*, vol. **188**, pp. 611–639, 2003.

Brackbill, J., Kothe, D., and Zemach, C., A Continuum Method for Modeling Surface Tension, *J. Comput. Phys.*, vol. **100**, pp. 335–354, 1992.

Briffa, F.E. and Dombrowski, N., Entrainment of Air into a Liquid Spray, *AIChE J.*, vol. **12**, no. 4, pp. 708–717, 1966.

Chiodi, R. and Desjardins, O., A Reformulation of the Conservative Level Set Reinitialization Equation for Accurate and Robust Simulation of Complex Multiphase Flows, *J. Comput. Phys.*, vol. **343**, pp. 186–200, 2017.

Desantes, J., Payri, R., Salvador, F., and Gil, A., Development and Validation of a Theoretical Model for Diesel Spray Penetration, *Fuel*, vol. **85**, no. 7, pp. 910–917, 2006.

Deshpande, S., Gao, J., and Trujillo, M.F., Characteristics of Hollow Cone Sprays in Crossflow, *Atomization Sprays*, vol. **21**, no. 4, pp. 349–361, 2011.

Deshpande, S.S., Anumolu, L., and Trujillo, M.F., Evaluating the Performance of the Two-Phase Flow Solver interFoam, *Comput. Sci. Discovery*, vol. **5**, no. 1, p. 014016, 2012.

Eroglu, H., Chigier, N., and Farago, Z., Coaxial Atomizer Liquid Intact Lengths, *Phys. Fluids A: Fluid Dynamics (1989-1993)*, vol. **3**, no. 2, pp. 303–308, 1991.

Faeth, G., Hsiang, L.P., and Wu, P.K., Structure and Breakup Properties of Sprays, *Int. J. Multiphase Flow*, vol. **21**, pp. 99–127, 1995.

Francois, M.M., Cummins, S.J., Dendy, E.D., Kothe, D.B., Sicilian, J.M., and Williams, M.W., A Balanced-Force Algorithm for Continuous and Sharp Interfacial Surface Tension Models within a Volume Tracking Framework, *J. Comput. Phys.*, vol. **213**, pp. 141–173, 2006.

Gopala, V.R. and van Wachem, B.G.M., Volume of Fluid Methods for Immiscible-Fluid and Free-Surface Flows, *Chem. Eng. J.*, vol. **141**, pp. 204–221, 2008.

Herrmann, M., Arienti, M., and Soteriou, M., The Impact of Density Ratio on the Primary Atomization of a Turbulent Liquid Jet in Crossflow, *ASME Turbo Expo 2010: Power for Land, Sea, and Air*, American Society of Mechanical Engineers, pp. 823–832, 2010.

Hiroyasu, H., Shimizu, M., and Arai, M., The Breakup of High Speed Jet in a High Pressure Gaseous Atmosphere, *Proc. 2nd Int. Conf. on Liquid Atomization and Spray Systems*, Institute of Liquid Atomization and Spray Systems, Pittsburgh PA, pp. 69–74, 1988.

Issa, R.I., Solution of the Implicitly Discretised Fluid Flow Equations by Operator Splitting, *J. Comput. Phys.*, vol. **62**, pp. 40–65, 1986.

Jarrahbashi, D. and Sirignano, W., Vorticity Dynamics for Transient High-Pressure Liquid Injection, *Phys. Fluids*, vol. **26**, no. 101304, pp. 1–52, 2014.

Kastengren, A.L., Tilocco, F.Z., Duke, D.J., Powell, C.F., Zhang, X., and Moon, S., Time-Resolved X-ray Radiography of Sprays from Engine Combustion Network Spray a Diesel Injectors, *Atomization Sprays*, vol. **24**, no. 3, 2014.

Ling, Y., Fuster, D., Zaleski, S., and Tryggvason, G., Spray Formation in a Quasiplanar Gas-Liquid Mixing Layer at Moderate Density Ratios: a Numerical Closeup, *Phys. Rev. Fluids*, vol. **2**, no. 014005, 2017.

Linne, M., Paciaroni, M., Hall, T., and Parker, T., Ballistic Imaging of the near Field in a Diesel Spray, *Experiments Fluids*, vol. **40**, no. 6, pp. 836–846, 2006.

OpenFOAM User Guide, The Open Source CFD Toolbox User Guide, Version 1.5, OpenCFD Limited, 2008.

Payri, R., Salvador, F., Gimeno, J., and Garcia, A., Flow Regime Effects over Non-Cavitating Diesel Injection Nozzles, *Proc. IMechE Part D: J. Automobile Engineering*, vol. **226**, pp. 133–144, 2011.

Pilliod, J.E. and Puckett, E.G., Second-Order Accurate Volume-of-Fluid Algorithms for Tracking Material Interfaces, *J. Comput. Phys.*, vol. **199**, pp. 465–502, 2004.

Prosperetti, A. and Tryggvason, G., *Computational Methods for Multiphase Flow*, Cambrdige, U.K.: Cambridge University Press, 2009.

Reitz, R. and Bracco, F., Mechanisms of Breakup of Round Liquid Jets, *Encyclopedia of Fluid Mechanics*, vol. **3**, pp. 233–249, 1986.

Ricou, F.P. and Spalding, D., Measurements of Entrainment by Axisymmetrical Turbulent Jets, *J. Fluid Mech.*, vol. **11**, no. 1, pp. 21–32, 1961.

Rider, W.J. and Kothe, D.B., Reconstructing Volume Tracking, *J. Comput. Phys.*, vol. **141**, pp. 112–152, 1998.

Rusche, H., Computational Fluid Dynamics of Dispersed Two-Phase Flows at High Phase Fractions, PhD thesis, Imperial College of Science, Technology and Medicine, 2002.

Sethian, J.A. and Smereka, P., Level Set Methods for Fluid Interfaces, *Annu. Rev. Fluid Mech.*, vol. **35**, pp. 341–372, 2003.

Shinjo, J. and Umemura, A., Simulation of Liquid Jet Primary Breakup: Dynamics of Ligament and Droplet Formation, *Int. J. Multiphase Flow*, vol. **36**, no. 7, pp. 513–532, 2010.

Shinjo, J. and Umemura, A., Detailed Simulation of Primary Atomization Mechanisms in Diesel Jet Sprays (Isolated Identification of Liquid Jet Tip Effects), *Proc. Combustion Institute*, vol. **33**, no. 2, pp. 2089–2097, 2011a.

Shinjo, J. and Umemura, A., Surface Instability and Primary Atomization Characteristics of Straight Liquid Jet Sprays, *Int. J. Multiphase Flow*, vol. **37**, no. 10, pp. 1294–1304, 2011b.

Sussman, M. and Puckett, E.G., A Coupled Level Set and Volume-of-Fluid Method for Computing 3D and Axisymmetric Incompressible Two-Phase Flows, *J. Comput. Phys.*, vol. **162**, pp. 301–337, 2000.

Trujillo, M.F. and Parkhill, A.E., A Local Lagrangian Analysis of Passive Particle Advection in a Gas Flow Field, *Int. J. Multiphase Flow*, vol. **37**, pp. 1201–1208, 2011.

Tryggvason, G., Scardovelli, R., and Zaleski, S., *Direct Numerical Simulations of Gas-Liquid Multiphase Flows*, Cambridge, U.K.: Cambridge University Press, 2011.

Van Leer, B., Towards the Ultimate Conservative Difference Scheme. II. Monotonicity and Conservation Combined in a Second-Order Scheme, *J. Comput. Phys.*, vol. **14**, no. 4, pp. 361–370, 1974.

Wang, Y., Liu, X., Im, K.S., Lee, W.K., Wang, J., Fezzaa, K., Hung, D.L., and Winkelman, J.R., Ultrafast X-ray Study of Dense-Liquid-Jet Flow Dynamics using Structure-Tracking Velocimetry, *Nature Phys.*, vol. **4**, no. 4, pp. 305–309, 2008.

Xiao, F., Ii, S., and Chen, C., Revisit to the THINC Scheme: A Simple Algebraic VOF Algorithm, *J. Comput. Phys.*, vol. **230**, pp. 7086–7092, 2011.

Zandian, A., Sirignano, W., and Hussain, F., Planar Liquid Jet: Early Deformation and Atomization Cascades, *Phys. Fluids*, vol. **29**, no. 062109, 2017.

Zhao, H., *Advanced Direct Injection Combustion Engine Technologies and Development: Diesel Engines*, Vol. 2, Cambridge, U.K.: Elsevier, 2009.

APPENDIX A. VALIDATION OF VOF SOLVER

The experiments employed in the current validation were reported by Eroglu et al. (1991) and consists of water injected through a cylindrical nozzle into a co-flowing stream of air. The liquid

injection speed is maintained at $U_j = 1.5$ m/s, while the speed of the surrounding gas stream (U_G) is systematically varied between different injection cases. The inner diameter of the nozzle (D) is 0.971 mm and the outer diameter is 1.262 mm. The fluid properties for the gas and liquid are, respectively, $\rho_G = 1.2$ kg/m^3, $\nu_G = 1.5 \times 10^{-5}$ m^2/s, $\rho_L = 1000$ kg/m^3, and $\nu_L = 10^{-6}$ m^2/s, with a surface tension coefficient of $\sigma = 0.07$ N/m. The key non-dimensional quantities are $\mathrm{Re}_L = \rho_L U_j D/\mu_L$ and $We_G = \rho_G (U_G - U_j)^2 D/2\sigma$.

Simulations were performed for $We_G = (13, 26, 50, 70, 100, 126,$ and $260)$ with a computational grid having a resolution of $\Delta x = 0.035$ mm ($D/\Delta x = 28$). This grid resolution was chosen to ensure numerically converged predictions of liquid core length. Visualization of a typical result is shown in Fig. A1, where the blue (darker) and gray (lighter) colors identify the unbroken jet core and broken liquid segments, respectively.

The intact liquid core length (X_{liq}) can be quantified by using a methodology similar to that of the electrical resistivity approach of Hiroyasu et al. (1988). Computationally, a parabolic equation is solved for a charge-like variable with a source at the nozzle, and a conductivity, which is non-zero only in the liquid phase. The solution of this equation provides instantaneous information on the unbroken liquid core, from which its length can be readily obtained. Figure A2 shows a history of X_{liq} for the case of U_G = 124.5 m/s ($We_G = 126$). The intact core length varies rapidly over time, and this corroborates the photographic observations of Eroglu et al. (1991).

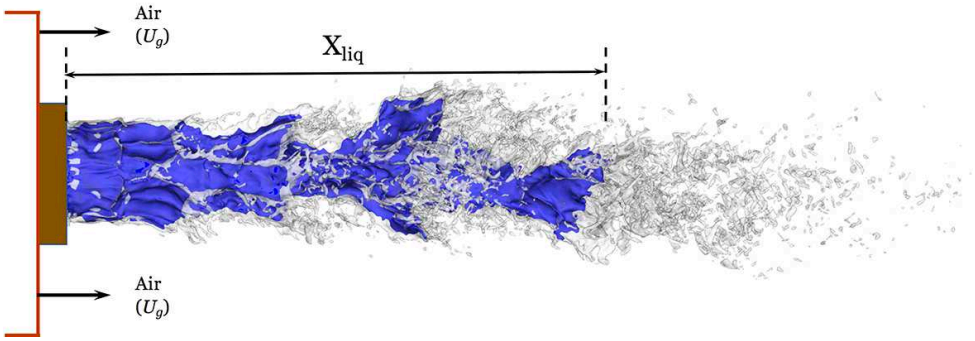

FIG. A1: Instantaneous visualization of the co-flow jet undergoing atomization

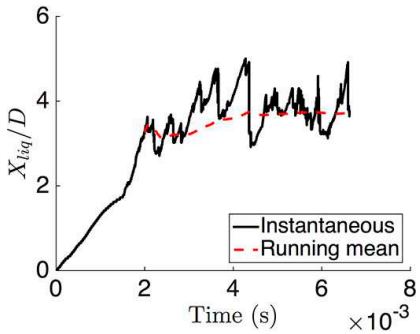

FIG. A2: Time history of $X_{liq}(t)$ for the co-flow jet exercise

The breakup occurs about a mean location, which is calculated as

$$\langle X_{liq} \rangle = \frac{1}{t_f - t_i} \int_{t_i}^{t_f} X_{liq}(t')dt', \tag{A.1}$$

where t_i reflects the time of first breakup (0.002 s in Fig. A2), and t_f is sufficiently long to yield a statistically converged mean value. The comparisons between $\langle X_{liq} \rangle$ and the experimental observations are presented in Fig. A3 for the different Weber numbers considered. Over this entire range of conditions, good agreement is achieved between the simulations and the experiments.

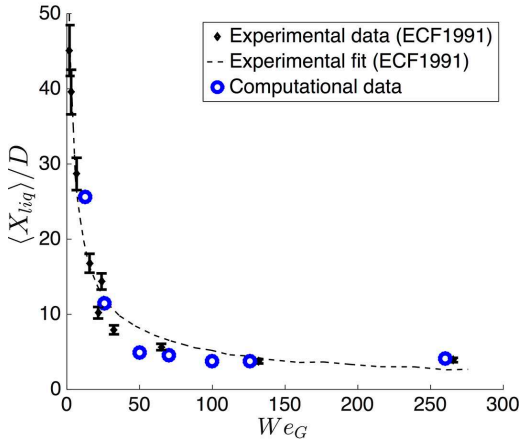

FIG. A3: Co-flow atomization showing a comparison of mean breakup length predictions with experiments (Eroglu et al., 1991)